Research Article Vol. 5, No. 7 / July 2018 / Optica 844

Three-dimensional spatially resolved optical energy density enhanced by wavefront shaping

Peilong Hong,[1,2,†] Oluwafemi S. Ojambati,[1,3,†] Ad Lagendijk,[1] Allard P. Mosk,[1,4] and Willem L. Vos[1,*]

[1]Complex Photonic Systems (COPS), MESA + Institute for Nanotechnology, University of Twente, P.O. Box 217, 7500 AE Enschede, The Netherlands
[2]Present address: Faculty of Science, Ningbo University, Ningbo 315211, China
[3]Present address: NanoPhotonics Center, Cavendish Laboratory, University of Cambridge, UK
[4]Present address: Nanophotonics, Debye Institute, Utrecht University, P.O. Box 80.000, 3508 TA Utrecht, The Netherlands
*Corresponding author: w.l.vos@utwente.nl

Received 18 December 2017; revised 21 March 2018; accepted 5 April 2018 (Doc. ID 317984); published 12 July 2018

While a three-dimensional (3D) scattering medium is from the outset opaque, such a medium sustains intriguing transport channels with near-unity transmission that are pursued for fundamental reasons and for applications in solid-state lighting, random lasers, solar cells, and biomedical optics. Here, we study the 3D spatially resolved distribution of the energy density of light in a 3D scattering medium upon the excitation of highly transmitting channels. The coupling into these channels is excited by spatially shaping the incident optical wavefronts to a focus on the back surface. To probe the local energy density, we excite isolated fluorescent nanospheres distributed inside the medium. From the spatial fluorescent intensity pattern we obtain the position of each nanosphere, while the total fluorescent intensity gauges the energy density. Our 3D spatially resolved measurements reveal that the differential fluorescent enhancement changes with depth, up to 26 × at the back surface of the medium, and the enhancement reveals a strong peak versus transverse position. We successfully interpret our results with a newly developed 3D model without adjustable parameters that considers the time-reversed diffusion starting from a point source at the back surface.

OCIS codes: (110.7050) Turbid media; (110.0113) Imaging through turbid media; (110.1080) Active or adaptive optics; (090.2880) Holographic interferometry; (110.7348) Wavefront encoding.

https://doi.org/10.1364/OPTICA.5.000844

1. INTRODUCTION

The interference of multiple scattered waves in complex media holds much fascinating physics such as coherent backscattering, Anderson localization, and mesoscopic correlations [1–4]. Transport through complex media is described by so-called channels that are eigenmodes of the transmission matrix [5]. Remarkably, open transmission channels with near-unity transmission are predicted to perfectly transmit a properly designed incident field even if the medium is optically thick [6]. It has recently been demonstrated that light is sent preferentially into a combination of open and highly transmitting channels by the spatial shaping of the incident wavefronts [7–9]. This development has led to tightly focused transmitted light (henceforth referred to as "optimized light") [10–13], focusing inside a scattering medium [14,15], enhanced optical transport through a scattering medium [7,8,16–18], sending an image through a scattering medium [19], and imaging inside a scattering medium [20–22].

In contrast, only a few studies address the energy density of optimized light that plays a central role in diverse applications of light–matter interactions, such as solid-state lighting [23,24], random lasers [25], solar cells [26], biomedical optics [27], or control of fluorescent proteins [28]. In the absence of wavefront control, the ensemble-averaged energy density depends linearly on depth z in the medium [1]. The critical questioning is how can the energy density be controlled by exciting open channels, and what is the resulting three-dimensional (3D) energy density. In particular, the 3D energy density profile of shaped light has not been experimentally studied to date. Due to the inherent opacity, direct optical imaging cannot be used to probe the 3D energy density profile. In Ref. [29], it was shown that spontaneous emission of embedded fluorescent nanoparticles does report the energy density, and it was observed that the depth-integrated *global* energy density is increased by wavefront shaping but the 3D profile could not be resolved. Several studies on low-dimensional systems [30–36] indicate that the energy density versus z position has a maximum near the center of the sample, while the transverse (x, y) dependence was not addressed. Thus, to investigate how the 3D local optical energy density is controlled by wavefront shaping, a *local* 3D (x, y, z)-resolved measurement is called for.

In this work, we investigate the 3D *local* spatially resolved energy density in a 3D scattering medium, with optimized incident light. Figure 1 illustrates our experiment: using a spatial light modulator (SLM), we shape the incident green light to a focus at the back surface of a disordered ensemble of ZnO nanoparticles,

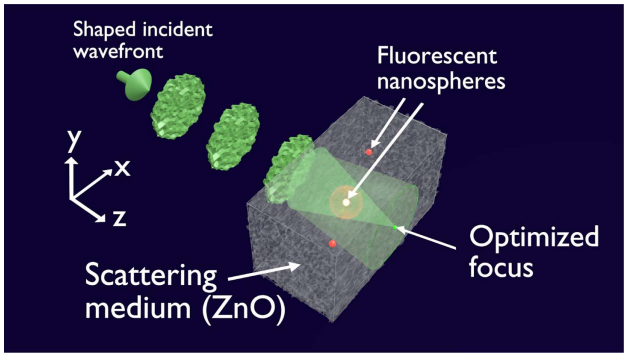

Fig. 1. Schematic of our method to probe the 3D (x, y, z) spatially resolved local energy density that is enhanced by wavefront shaping. Incident green light is wavefront shaped to an optimized focus at the back surface of a scattering medium (ensemble of ZnO nanospheres) to preferentially excite open transmission channels. The scattering medium is sparsely doped with fluorescent nanospheres that probe the local energy density of the green incident light at different positions (x, y, z) by emitting orange light in proportion to the local energy density of the green excitation light.

a procedure that is known to enhance the coupling of light into highly transmitting channels [7,30,31,34]. The resulting energy density is probed *locally* by fluorescent nanospheres. The density of the nanospheres is so low that only one of them is present in the illuminated volume. Wavefront shaping increases the local energy density by an enhancement factor that we denote as $\eta_f(x, y, z)$. Consequently, the fluorescence emission of a nanosphere, which is proportional to the local energy density at its location, is enhanced by the same factor. We performed measurements on several nanospheres inside a sample, and for each individual sphere we measured two key parameters, namely, the nanosphere location (x, y, z) and the differential fluorescence enhancement $\partial\eta_f/\partial F$. Here the fidelity F quantifies the overlap between the experimentally generated wavefront and the perfect wavefront that optimally couples light to the target position [7].

2. MAIN OBSERVATION

Figures 2 and 3 show our main results: the *measured* differential fluorescence enhancement $\partial\eta_f/\partial F$ versus depth and transverse position, respectively, in scattering samples with thicknesses of $L = 8 \pm 2$ μm and 16 ± 2 μm [37]. In Fig. 2, $\partial\eta_f/\partial F$ increases with depth z from front to back, and $\partial\eta_f/\partial F$ increases up to 16 and 26 with thickness L. In the hypothetical situation where control of the incident light does not systematically change the internal energy density we would find $\partial\eta_f/\partial F = 0$. The data deviate strongly from this condition, which shows that the energy density is strongly controlled. We propose a 3D model without free parameters that describes the data in Fig. 2 very well.

To verify the 3D character of $\eta_f(x, y, z)$, we translate the sample transversely along the x axis at constant depth. Figure 3 shows the differential fluorescence enhancement $\partial\eta_f/\partial F$ versus the transverse displacement relative to the optical axis (x_0, y_0). For both samples, $\partial\eta_f/\partial F$ reveals clear maxima, revealing the effect of the optimized focus [38]. Due to cylindrical symmetry in the transverse plane, similar behavior occurs versus both x and y, thus, scanning the y coordinate [or even combinations $(x + y)$ or $(x - y)$, etc.] is completely equivalent. The surface map in

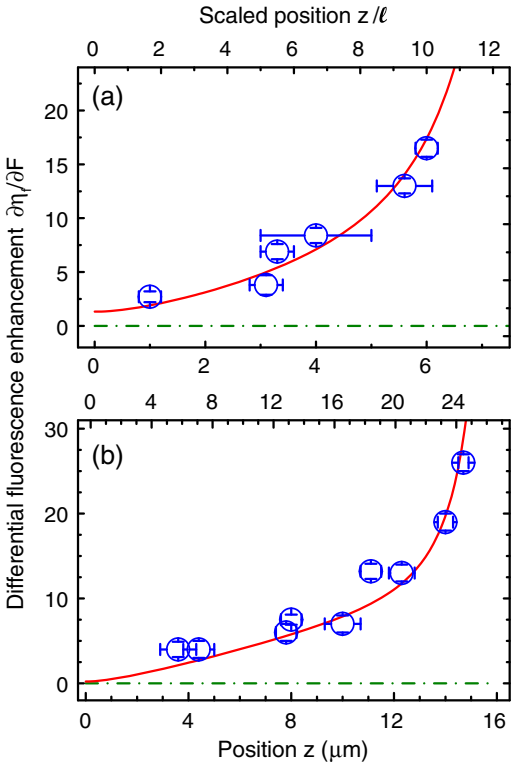

Fig. 2. Measured differential fluorescence enhancement $\partial\eta_f/\partial F$ (blue circles with error bars) versus depth z and scaled depth z/ℓ for two samples with thicknesses of (a) $L = 8$ μm and (b) $L = 16$ μm. The vertical error bars are comparable to the symbol size. The fluorescent nanospheres are centered on the optical axis at (x_0, y_0). The red curve is the energy density enhancement predicted by our 3D model. The green dashed–dotted curve indicates a hypothetical absence of control of the energy density.

Fig. 3 shows the cylinder-symmetric transverse distribution with the measured data points. The observed strong dependence on the transverse coordinate is also well described by our 3D model, while it is not explained at all by previous 1D diffusion models that are necessarily independent of (x, y) [30–36].

3. EXPERIMENTAL METHODS

A. Samples

The samples were prepared by spray painting a suspension of ZnO nanoparticles and a low concentration of fluorescent particles on a glass slide (details in Supplement 1). After evaporation, we obtained a dense ensemble of strongly scattering ZnO nanoparticles, with a transport mean-free path of $\ell = 0.58^{+0.16}_{-0.10}$ μm. The thickness L of the sample was controlled by the spraying time, and we made 8 μm and 16 μm thick samples. Since the lateral (x, y) extent of our samples (3 mm) is much greater than the thickness and since the thickness is much greater than the mean-free path, the photon transport in the samples is truly 3D.

B. Determination of the Depth of the Nanoparticle

The locations (x, y, z) of the fluorescent nanospheres are *a priori* unknown since the nanospheres end up at random positions. To determine the locations (x, y, z), we first scanned the sample to find isolated fluorescent spheres and then recorded the diffuse

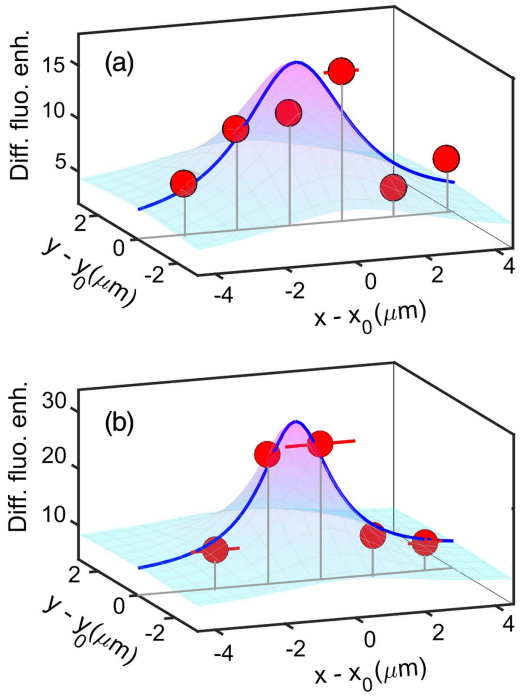

Fig. 3. Differential fluorescence enhancement $\partial\eta_f/\partial F$ versus transverse displacement Δx relative to the optical axis for scattering samples with thicknesses of (a) $L = 8$ μm [nanosphere at $(y, z) = (0, 5.9 \pm 0.1)$ μm] and (b) $L = 16$ μm [nanosphere at $(y, z) = (0, 14.7 \pm 0.2)$ μm]. Red circles are the measured data with error bars. The light blue surface map and the blue solid line are the differential energy densities along the transverse x position at $y = 0$, as predicted by our 3D model.

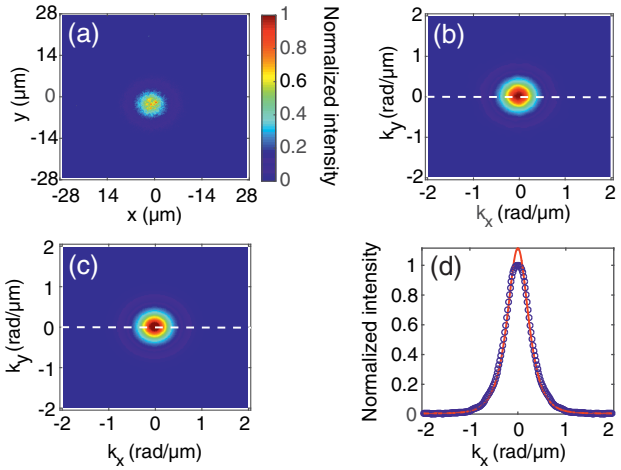

Fig. 4. Determining the depth z of a fluorescent sphere in the $L = 8$ μm sample. (a) Fluorescence image measured in real space by averaging $m_1 = 41$ data sets, each with a different random incident wavefront. (b) Fourier transform of the data in panel (a). Intensities in (a) and (b) are normalized to their maxima. (c) Solution of the diffusion equation with a single fluorescent nanosphere at depth $z = 3.3 \pm 0.3$ μm. (d) Cross sections through the centers of (b) (blue circles) and (c) (red line), respectively, showing a good match.

fluorescent spot at the back surface of the sample [see Fig. 4(a)]. We performed a Fourier transformation of the fluorescent spot [see Fig. 4(b)] and filtered high-frequency noise. We model the nanosphere as a point source in the 3D diffusion equation [14] and fit the solution in Fourier space to the Fourier transform of the fluorescence spot with the nanosphere depth z as the only adjustable parameter; see Figs. 4(c)–4(d). For the particular fluorescent nanosphere shown in Fig. 4, the depth is $z = 3.3 \pm 0.3$ μm. To determine the z-error bar, we performed 100 measurements on a single nanosphere. Since the measured fluorescent intensity varies for the 100 measurements, the mean and standard deviation over the 100 measurements give z and z-error bar, respectively. The variation in the z-error bars from each nanosphere in Figs. 2 and 3 is probably because different nanospheres reveal different intensities (e.g., due to different doping or bleaching).

C. Wavefront Shaping and Fidelity

Next, we performed wavefront shaping experiments with the optical axis of the system centered on a nanosphere at coordinates (x_0, y_0). We obtained a feedback signal for the wavefront shaping optimization from an area of 0.03 μm^2, which is smaller than the speckle area $A = \lambda_c^2/(2\pi) = 0.05$ μm^2. The output beam diameter is estimated to be about 56 μm for an unoptimized incident wavefront, corresponding to order of magnitude 10^4 transmission channels. We used the piecewise sequential algorithm to find the optimized incident wavefront [7,10], with $N = 900$ input degrees of freedom on the spatial light modulator, as discussed in Supplement 1.

Ideally, a perfectly shaped wavefront is the phase conjugate of the wavefront originating from a point source located at the target position [7]. A real wavefront in an experiment inevitably differs from a perfect wavefront due to finite resolution, temporal decoherence, modulation noise, and spatial extent of the generated field [7,10,39]. The deviation of the wavefront from the ideal one due to all these effects can be represented in a single measure: the fidelity F (that is the same as $|\gamma|^2$ in Refs. [7,29]). Experimentally, the fidelity F is gauged as $F = n^2 \cdot I_{opt}/I_{tot}$, where n is the refractive index of the substrate, I_{opt} the intensity for the optimized wavefront, and I_{tot} the total transmitted intensity with an unoptimized reference wavefront [7,29]. Since a real wavefront is the superposition of the perfectly shaped wavefront that controls the energy density and a random error wavefront [7], the energy density $W_e(x, y, z)$ due to a real incident wavefront is necessarily a linear combination of the perfectly optimized energy density $W_o(x, y, z)$ and a diffusive unoptimized energy density $W_{uo}(x, y, z)$

$$W_e(x, y, z) = F \cdot W_o(x, y, z) + (1 - F) \cdot W_{uo}(x, y, z). \quad (1)$$

[The energy densities in Eq. (1) are ensemble averaged; see Supplement 1]. By probing the fluorescent spheres at different positions, we obtain the local energy density enhancement defined as $\eta_f(x, y, z) \equiv W_e(x, y, z)/W_{uo}(x, y, z)$. Equation (1) leads to a linear dependence of the energy density enhancement on fidelity:

$$\eta_f(x, y, z) = 1 + F \cdot \frac{\partial \eta_f}{\partial F}, \quad (2)$$

with *unity* intercept and a slope $\partial\eta_f/\partial F = (W_o/W_{uo} - 1)$ that we call the *differential fluorescent enhancement* [40].

D. Controlling Fidelity

To determine $\partial\eta_f/\partial F$ from Eq. (2), it is necessary to control the fidelity. Therefore, we systematically perturbed the optimized wavefront by adding to each pixel a random phase noise. The perturbed optimized pattern $\phi_p(i,j)$ is expressed as

$$\phi_p(i,j) = \phi_o(i,j) + \delta\phi(i,j), \tag{3}$$

where the indices (i,j) are the segments on the spatial light modulator (SLM), $\phi_o(i,j)$ is the optimized phase pattern, and $\delta\phi(i,j)$ is the phase noise that takes random values between zero and a maximum value $\delta\phi_m$. We varied $\delta\phi_m$ from 0 to 2π in 41 steps, and we measured the fidelity for each phase perturbation. We expect that the phase noise gradually reduces the fidelity, which is indeed observed in Fig. 5. For each perturbed phase we collected a fluorescence image I_p and $m_1 = 41$ reference fluorescent images I_r, each with a random incident wavefront. (I_p and I_r are integrated over all camera pixels within the fluorescent peak). We determined experimentally the fluorescence enhancement η_f from the ratio of I_p and the average I_r. We repeated the wavefront shaping and fidelity scanning procedure $m_2 = 100$ times on each nanosphere to obtain an ensemble average.

The measured collection of $(m_1 \cdot m_2 = 4100)$ fluorescence enhancement η_f data points versus fidelity F is shown in Fig. 6 for one fluorescent nanosphere. While the data show inevitable variations, which are primarily due to a low-signal-to-noise ratio from the intensity of single nanosphere (see Supplement 1), the fluorescence enhancement clearly increases with F, to an average of 1.4× at the maximum fidelity, as confirmed by the rebinned data. From the linear dependence between η_f and F with unity axis intercept [see Eq. (2)], we obtain the slope $\partial\eta_f/\partial F$ that is directly obtained from the data, without any extrapolation. The procedure above was done both versus depth and versus transverse position, and all resulting differential fluorescence enhancements $\partial\eta_f/\partial F$ are shown in Figs. 2 and 3.

4. THEORY AND DISCUSSION

To model the 3D energy density $W_o(x,y,z)$ of optimized light, we consider the optimized target to be a point source of diffuse light, as shown in Fig. 1. The 3D energy density $W_{dif}(x,y,z)$ of the point source is described by the 3D diffusion equation [1,14] (for details, see Supplement 1). Light from the point source diffuses in a cone from the back surface to the front surface,

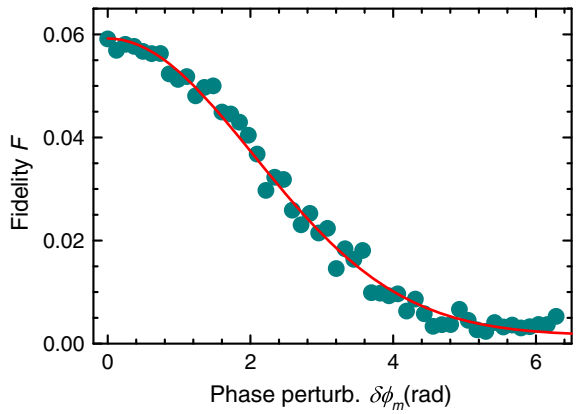

Fig. 5. Measured fidelity F versus the phase perturbation factor $\delta\phi_m$ on the optimized phase pattern. The red curve is a guide to the eye.

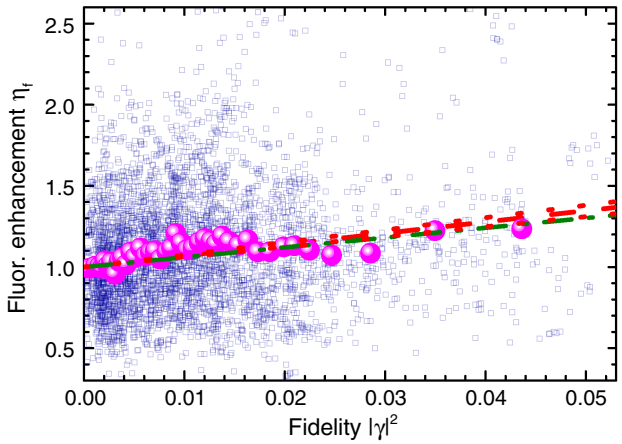

Fig. 6. Measured fluorescence enhancement η_f versus fidelity F (blue squares) at a depth $z = 3.3 \pm 0.3$ μm in the $L = 8$ μm thick sample. Red dashed line: Eq. (2) with unity intercept and differential fluorescence enhancement $\partial\eta_f/\partial F = 6.9 \pm 0.7$ as the only adjustable parameter, with the error at the 95% confidence interval (red dotted lines). Magenta circles are rebinned data (101 raw data per bin), which give a similar result: $\partial\eta_f/\partial F = 6.7 \pm 0.6$ (green dashed–dotted line).

preferentially via open channels. While the time reverse (or phase conjugate) of the light transmitted to the front surface describes light traveling to the target point at the back surface, part of the light injected at the front surface contributes to a background, notably in the space outside the optimized focus (see Fig. 1). This background originates from the fact that open channels do not form a complete basis and hence cannot compose an ideal background-free focus [7,31]. Therefore, at perfect fidelity we describe the optimized energy density $W_o(x,y,z)$ as a sum of two components:

$$W_o(x,y,z) = W_{of}(x,y,z) + W_{bg}(x,y,z), \tag{4}$$

with W_{of} the energy density originating from the optimized focus, and W_{bg} the background energy density. Following the maximal fluctuation approximation by Pendry *et al.*, we describe W_{of} and W_{bg} by assuming that the transmission channels consist of only open and closed channels [41,42]. For open channels, it has recently been shown that the energy density profile along z tracks the fundamental mode of the diffusion equation [29,34,36]. To obtain W_{of}, we normalize $W_{dif}(x,y,z)$ and map its z dependence onto the spatial profile of the fundamental diffusion mode $W_{m=1}$ (see Supplement 1). Similarly, we describe W_{bg} by mapping the fundamental diffusion mode onto a Gaussian profile with a constant width along z. The amplitudes of W_{fo} and W_{bg} are fixed by the total transmitted intensity.

In our experiments, a fluorescent nanosphere at position (x,y,z) is excited by the local energy density $W_o(x,y,z)$ in the case of optimized light (modeled above) or $W_{uo}(x,y,z)$ for unoptimized incident light. We describe $W_{uo}(x,y,z)$ as a product of the solution of the 1D diffusion equation (versus z) and a Gaussian [in (x,y)]. Figure 7(a) shows the energy density of optimized light at various depths calculated using Eq. (4) (see Supplement 1). The energy density first spreads until about $z = 3$ μm and converges to a focus at the back surface of the sample. These energy densities also serve to interpret transverse scans as in Fig. 3: the scan in Fig. 3(a) taken near $z = 6$ μm in the

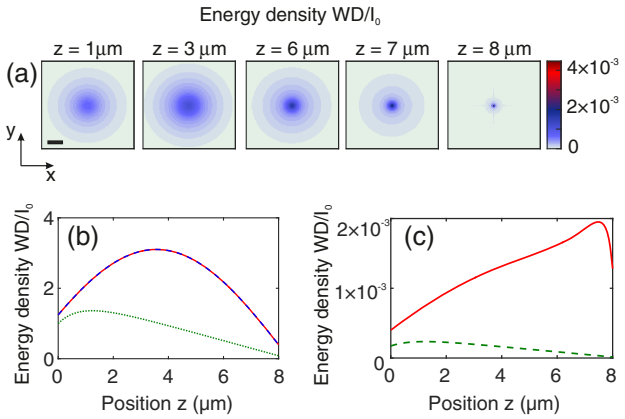

Fig. 7. (a) Transverse (x, y) cross sections of the calculated energy densities of optimized light at various depths z inside a scattering medium with thickness $L = 8$ μm. The scale bar is 10 μm. (b) Energy densities of optimized light W_o integrated over the transverse (x, y)-plane (red solid curve), unoptimized light W_{uo} (green short-dashed curve), and the energy density of the fundamental diffusion mode $W_{m=1}$ as a function of depth z. (c) The energy densities $W_o(x = 0, y = 0, z)$ (red solid curve) and $W_{uo}(x = 0, y = 0, z)$ (green dashed curve) as a function of z. I_0 and D are the incident intensity and the diffusion constant, respectively.

$L = 8$ μm sample has a width of about 3 μm, which agrees well with the calculated results in Fig. 7(a) (middle panel).

Figure 7(b) shows the (x, y)-integrated energy densities W_o, W_{uo}, and $W_{m=1}$ as functions of position z. The figure reveals that W_o matches with $W_{m=1}$, both having a peak close to the center of the sample and decreasing toward the sample surfaces. The agreement of the two functions is expected since $W_{m=1}$ is translationally invariant along (x, y). In addition, we find that both W_o and $W_{m=1}$ are enhanced compared to the unoptimized density W_{uo}, as shown earlier [29]. Figure 7(c) shows the energy densities of optimized and unoptimized light on the optical axis at $(x, y) = (0,0)$. $W_o(x = 0, y = 0, z)$ increases steadily and has a maximum close to the back surface of the sample. The peak close to the back surface of the sample is attributed to the position of the point source at $z = L - \ell$ in the solution of the diffusion equation. In contrast, $W_{uo}(x = 0, y = 0, z)$ increases only slightly until around $z = 1$ μm and then decreases toward the back surface of the sample. To the best of our knowledge, this is the first description of the energy density of wavefront-shaped light in 3D.

From the ratio of W_o and W_{uo}, we obtain differential fluorescence enhancement $\partial\eta_f/\partial F$ [see Eqs. (S11)–(S14)] that is plotted as a function of depth z in Fig. 2. For both samples, our 3D model shows that $\partial\eta_f/\partial F$ increases steadily as z increases to the back surface of the sample, in excellent agreement with the experimental data. The steady increase is mainly due to the focusing of the energy density of optimized light W_o, as shown in Fig. 7(a). Figures 2(a) and 2(b) also show that the twice thicker sample has about twice greater differential fluorescence enhancement $\partial\eta_f/\partial F$. This effect was observed for many fluorescent particles inside the scattering medium [29]. We attribute the dependence of the fluorescence enhancement on sample thickness to the fluorescent enhancement being determined by the ratio of optimized and unoptimized intensities, the latter decreasing linearly versus depth; see Fig. 7(b). Both agreements show that the intensity enhancement observed on the back surface is associated with the 3D enhancement of the local energy density in the bulk of the scattering medium.

5. SUMMARY

By exciting highly transmitting channels in a 3D scattering medium by wavefront shaping, we observe that the local energy density is considerably enhanced. The enhancement increases toward the back surface of the sample and has a maximum along the transverse direction, revealing the effect of the optimized focus. A 3D model without adjustable parameters successfully describes the experimental data. Our results thus offer new insights on the 3D redistribution of the energy density in 3D scattering media, which is extremely useful to enhance the efficiency of energy conversion in systems such as random lasers, solar cells, and white LEDs. For white LEDs, wavefront shaping could serve to control the color temperature by optimizing for warm or cold white light. Our results also pertain to wavefront shaping of classical waves, such as acoustic and pressure waves [43], and to quantum waves, such as electrons in nanostructures.

Funding. Stichting voor Fundamenteel Onderzoek der Materie (FOM); Stichting voor de Technische Wetenschappen (STW); Defense Advanced Research Projects Agency (DARPA); Nederlandse Organisatie voor Wetenschappelijk Onderzoek (NWO).

Acknowledgment. We thank Cornelis Harteveld for technical help and Jeremy Baumberg, Sylvain Gigan, Pepijn Pinkse, Stefan Rotter, Tristan Tentrup, Wilbert IJzerman, and Floris Zwanenburg for discussions. This work is part of the research program of the "Stichting voor Fundamenteel Onderzoek der Materie" (FOM) FOM-program "Stirring of light!," which is part of the "Nederlandse Organisatie voor Wetenschappelijk Onderzoek" (NWO), and we acknowledge support by NWO-Vici, DARPA, NWO-TTW, and Rubicon fellowship.

†These authors contributed equally.

See Supplement 1 for supporting content.

REFERENCES AND NOTES

1. M. C. W. van Rossum and T. M. Nieuwenhuizen, "Multiple scattering of classical waves: microscopy, mesoscopy, and diffusion," Rev. Mod. Phys. **71**, 313–371 (1999).
2. P. Sheng, *Introduction to Wave Scattering, Localization, Mesoscopic Phenomena* (Springer, 2006).
3. E. Akkermans and G. Montambaux, *Mesoscopic Physics of Electrons and Photons* (Cambridge University, 2007).
4. D. S. Wiersma, "Disordered photonics," Nat. Photonics **7**, 188–196 (2013).
5. C. W. J. Beenakker, "Random-matrix theory of quantum transport," Rev. Mod. Phys. **69**, 731–808 (1997).
6. O. N. Dorokhov, "On the coexistence of localized and extended electronic states in the metallic phase," Solid State Commun. **51**, 381–384 (1984).
7. I. M. Vellekoop and A. P. Mosk, "Universal optimal transmission of light through disordered materials," Phys. Rev. Lett. **101**, 120601 (2008).
8. S. M. Popoff, A. Goetschy, S. F. Liew, A. D. Stone, and H. Cao, "Coherent control of total transmission of light through disordered media," Phys. Rev. Lett. **112**, 133903 (2014).
9. A. P. Mosk, A. Lagendijk, G. Lerosey, and M. Fink, "Controlling waves in space and time for imaging and focusing in complex media," Nat. Photonics **6**, 283–292 (2012).

10. I. M. Vellekoop and A. P. Mosk, "Focusing coherent light through opaque strongly scattering media," Opt. Lett. **32**, 2309–2311 (2007).
11. I. M. Vellekoop, A. Lagendijk, and A. P. Mosk, "Exploiting disorder for perfect focusing," Nat. Photonics **4**, 320–322 (2010).
12. O. Katz, E. Small, Y. Bromberg, and Y. Silberberg, "Focusing and compression of ultrashort pulses through scattering media," Nat. Photonics **5**, 372–377 (2011).
13. E. G. van Putten, D. Akbulut, J. Bertolotti, W. L. Vos, A. Lagendijk, and A. P. Mosk, "Scattering lens resolves sub-100 nm structures with visible light," Phys. Rev. Lett. **106**, 193905 (2011).
14. I. M. Vellekoop, E. G. van Putten, A. Lagendijk, and A. P. Mosk, "Demixing light paths inside disordered metamaterials," Opt. Express **16**, 67–80 (2008).
15. R. Horstmeyer, H. Ruan, and C. Yang, "Guidestar-assisted wavefront-shaping methods for focusing light into biological tissue," Nat. Photonics **9**, 563–571 (2015).
16. M. Kim, Y. Choi, C. Yoon, W. Choi, J. Kim, Q. Park, and W. Choi, "Maximal energy transport through disordered media with the implementation of transmission eigenchannels," Nat. Photonics **6**, 581–585 (2012).
17. W. Choi, M. Kim, D. Kim, C. Yoon, C. Fang-Yen, Q.-H. Park, and W. Choi, "Preferential coupling of an incident wave to reflection eigenchannels of disordered media," Sci. Rep. **5**, 11393 (2015).
18. O. S. Ojambati, J. T. Hosmer-Quint, K. J. Gorter, A. P. Mosk, and W. L. Vos, "Controlling the intensity of light in large areas at the interfaces of a scattering medium," Phys. Rev. A **94**, 043834 (2016).
19. S. Popoff, G. Lerosey, M. Fink, A. C. Boccara, and S. Gigan, "Image transmission through an opaque material," Nat. Commun. **1**, 81 (2010).
20. O. Katz, E. Small, and Y. Silberberg, "Looking around corners and through thin turbid layers in real time with scattered incoherent light," Nat. Photonics **6**, 549–553 (2012).
21. J. Bertolotti, E. G. van Putten, C. Blum, A. Lagendijk, W. L. Vos, and A. P. Mosk, "Non-invasive imaging through opaque scattering layers," Nature **491**, 232–234 (2012).
22. D. Psaltis and I. N. Papadopoulos, "The fog clears," Nature **491**, 197–198 (2012).
23. J. M. Phillips, M. E. Coltrin, M. H. Crawford, A. J. Fischer, M. R. Krames, R. Mueller-Mach, G. O. Mueller, Y. Ohno, L. E. S. Rohwer, J. A. Simmons, and J. Y. Tsao, "Research challenges to ultra-efficient inorganic solid-state lighting," Laser Photon. Rev. **1**, 307–333 (2007).
24. M. L. Meretska, A. Lagendijk, H. Thyrrestrup, A. P. Mosk, W. L. IJzerman, and W. L. Vos, "How to distinguish elastically scattered light from Stokes shifted light for solid-state lighting?" J. Appl. Phys. **119**, 093102 (2016).
25. N. M. Lawandy, R. M. Balachandran, A. S. L. Gomes, and E. Sauvain, "Laser action in strongly scattering media," Nature **368**, 436–438 (1994).
26. A. Polman and H. A. Atwater, "Photonic design principles for ultrahigh-efficiency photovoltaics," Nat. Mater. **11**, 174–177 (2012).
27. L. V. Wang and H. Wu, *Biomedical Optics: Principles and Imaging* (Wiley, 2012).
28. C. Blum, A. P. Mosk, I. S. Nikolaev, V. Subramaniam, and W. L. Vos, "Color control of natural fluorescent proteins by photonic crystals," Small **4**, 492–496 (2008).
29. O. S. Ojambati, H. Yılmaz, A. Lagendijk, A. P. Mosk, and W. L. Vos, "Coupling of energy into the fundamental diffusion mode of a complex nanophotonic medium," New J. Phys. **18**, 043032 (2016).
30. W. Choi, A. P. Mosk, Q. Park, and W. Choi, "Transmission eigenchannels in a disordered medium," Phys. Rev. B **83**, 134207 (2011).
31. M. Davy, Z. Shi, and A. Z. Genack, "Focusing through random media: eigenchannel participation number and intensity correlation," Phys. Rev. B **85**, 035105 (2012).
32. M. Davy, Z. Shi, J. Park, C. Tian, and A. Z. Genack, "Universal structure of transmission eigenchannels inside opaque media," Nat. Commun. **6**, 6893 (2015).
33. S. F. Liew and H. Cao, "Modification of light transmission channels by inhomogeneous absorption in random media," Opt. Express **23**, 11043 (2015).
34. O. S. Ojambati, A. P. Mosk, I. M. Vellekoop, A. Lagendijk, and W. L. Vos, "Controlling waves in space and time for imaging and focusing in complex media," Opt. Express **24**, 18525 (2016).
35. R. Sarma, A. G. Yamilov, S. Petrenko, Y. Bromberg, and H. Cao, "Control of energy density inside a disordered medium by coupling to open or closed channels," Phys. Rev. Lett. **117**, 086803 (2016).
36. M. Koirala, R. Sarma, H. Cao, and A. Yamilov, "Inverse design of perfectly transmitting eigenchannels in scattering media," Phys. Rev. B **96**, 054209 (2017).
37. Although the differential fluorescence enhancement (the slope) is proportional to the enhancement in the ideal limit of perfect fidelity [29], we focus here on the slope since it is directly obtained from the measurements.
38. In Figs. 3(a) and 3(b), the maxima are centered at $X_0 = 3\ \mu\mathrm{m}$ and $X_0 = 1\ \mu\mathrm{m}$, respectively, due to a slight misalignment of the nanosphere from the optical axis. This misalignment is due to the weakness of the signal from fluorescent particles that are close to the back surface of the sample.
39. H. Yılmaz, W. L. Vos, and A. P. Mosk, "Optimal control of light propagation through multiple-scattering media in the presence of noise," Biomed. Opt. Express **4**, 1759–1768 (2013).
40. Our procedure is an innovation beyond Ref. [29] where we extrapolated to perfect fidelity; the present one solely exploits measured quantities.
41. J. B. Pendry, A. MacKinnon, and A. B. Pretre, "Maximal fluctuations—a new phenomenon in disordered systems," Physica A **168**, 400–407 (1990).
42. J. B. Pendry, A. MacKinnon, and P. J. Roberts, "Universality classes and fluctuations in disordered systems," Proc. R. Soc. London Ser. A **437**, 67–83 (1992).
43. A. Derode, P. Roux, and M. Fink, "Robust acoustic time reversal with high-order multiple scattering," Phys. Rev. Lett. **75**, 4206–4209 (1995).